IVYSPRING INTERNATIONAL PUBLISHER

Theranostics

2018; 8(17): 4765-4780. doi: 10.7150/thno.25162

Research Paper

Simultaneous characterization of tumor cellularity and the Warburg effect with PET, MRI and hyperpolarized ^{13}C-MRSI

Christian Hundshammer[1,2,8*], Miriam Braeuer[1*], Christoph A. Müller[3,4,5*], Adam E. Hansen[6], Mathias Schillmaier[7], Stephan Düwel[1,2,8], Benedikt Feuerecker[1], Steffen J. Glaser[2], Axel Haase[8], Wilko Weichert[4,9], Katja Steiger[9,10], Jorge Cabello[1], Franz Schilling[1], Jan-Bernd Hövener[11], Andreas Kjær[6], Stephan G. Nekolla[1], Markus Schwaiger[1]✉

1. Department of Nuclear Medicine, Klinikum rechts der Isar, Technical University of Munich, 81675 München, Germany
2. Department of Chemistry, Technical University of Munich, 85748 Garching, Germany
3. Department of Radiology, Medical Physics, University Medical Center Freiburg, Faculty of Medicine, University of Freiburg, 79106 Freiburg, Germany
4. German Consortium for Cancer Research (DKTK), 69120 Heidelberg, Germany
5. German Cancer Research Center (DKFZ), 69120 Heidelberg, Germany
6. Department of Clinical Physiology, Nuclear Medicine & PET and Cluster for Molecular Imaging Rigshospitalet and University of Copenhagen, 2100 Copenhagen, Denmark
7. Department of Radiology, Klinikum rechts der Isar, Technical University of Munich, 81675 München, Germany
8. Munich School of Bioengineering, Technical University of Munich, 85748 Garching, Germany
9. Department of Pathology, Klinikum rechts der Isar, Technical University Munich, 81675 München, Germany
10. Comparative Experimental Pathology, Klinikum rechts der Isar, Technical University Munich, 81675 München, Germany
11. Section for Biomedical Imaging, Molecular Imaging North Competence Center (MOINCC), Department for Radiology and Neuroradiology, University Medical Center Kiel, University Kiel

*equal author contribution

✉ Corresponding author: Christian Hundshammer, Technical University of Munich, Klinikum rechts der Isar, Department of Nuclear Medicine, Ismaninger Str. 22, 81675 München, Germany. E-mail: christian.hundshammer@tum.de

Received: 2018.01.26; Accepted: 2018.06.26; Published: 2018.09.09

Abstract

Modern oncology aims at patient-specific therapy approaches, which triggered the development of biomedical imaging techniques to synergistically address tumor biology at the cellular and molecular level. PET/MR is a new hybrid modality that allows acquisition of high-resolution anatomic images and quantification of functional and metabolic information at the same time. Key steps of the Warburg effect-one of the hallmarks of tumors-can be measured non-invasively with this emerging technique. The aim of this study was to quantify and compare simultaneously imaged augmented glucose uptake and LDH activity in a subcutaneous breast cancer model in rats (MAT-B-III) and to study the effect of varying tumor cellularity on image-derived metabolic information.

Methods: For this purpose, we established and validated a multimodal imaging workflow for a clinical PET/MR system including proton magnetic resonance (MR) imaging to acquire accurate morphologic information and diffusion-weighted imaging (DWI) to address tumor cellularity. Metabolic data were measured with dynamic [^{18}F]FDG-PET and hyperpolarized (HP) ^{13}C-pyruvate MR spectroscopic imaging (MRSI). We applied our workflow in a longitudinal study and analyzed the effect of growth dependent variations of cellular density on glycolytic parameters.

Results: Tumors of similar cellularity with similar apparent diffusion coefficients (*ADC*) showed a significant positive correlation of FDG uptake and pyruvate-to-lactate exchange. Longitudinal DWI data indicated a decreasing tumor cellularity with tumor growth, while *ADC*s exhibited a significant inverse correlation with PET standard uptake values (*SUV*). Similar but not significant trends were observed with HP-^{13}C-MRSI, but we found that partial volume effects and point spread function artifacts are major confounders for the quantification of ^{13}C-data when the spatial resolution is

limited and major blood vessels are close to the tumor. Nevertheless, analysis of longitudinal data with varying tumor cellularity further detected a positive correlation between quantitative PET and ^{13}C-data.

Conclusions: Our workflow allows the quantification of simultaneously acquired PET, MRSI and DWI data in rodents on a clinical PET/MR scanner. The correlations and findings suggest that a major portion of consumed glucose is metabolized by aerobic glycolysis in the investigated tumor model. Furthermore, we conclude that variations in cell density affect PET and ^{13}C-data in a similar manner and correlations of longitudinal metabolic data appear to reflect both biochemical processes and tumor cellularity.

Key words: PET/MR, [^{18}F]FDG-PET, hyperpolarized ^{13}C-MRSI, DNP, diffusion-weighted imaging, multimodal imaging, NMR, spectroscopy

Introduction

The new paradigm in oncology is to tailor therapies for patient-specific phenotypes, which triggered the invention of powerful hybrid imaging modalities that address tumor biology in greater depth. PET/CT (position emission tomography/ computed tomography) has become commercially available at the beginning of this century and is currently the work-horse in clinical routine for diagnosis, staging, monitoring of response to treatment and outcome prediction of cancer patients. During the last decade, PET/MR has been introduced as a promising new hybrid modality that is potentially superior to PET/CT [1]. This is mainly because MR has an excellent soft-tissue contrast that is not available with CT and delivers accurate high-resolution anatomical images close to CT resolution and without additional radiation exposure. Furthermore, it allows quantitative functional imaging (fMRI), diffusion-weighted imaging (DWI) and metabolic imaging with hyperpolarized ^{13}C-labelled metabolites [2-5].

One of the main hallmarks of tumors that can be addressed non-invasively with metabolic imaging is the Warburg effect [6, 7]. Solid tumors consume abnormally high levels of glucose and catabolize it through inefficient glycolysis, which is an ubiquitous feature of tumors that malignant cells benefit from, e.g., through fast energy production [8]. Pyruvate is the final product of glycolysis and the nexus of the entire metabolic network. Even under normoxic conditions, it is mainly reduced to lactate by fermentation rather than oxidized [9-13].

2-deoxy-2-[^{18}]fluoro-D-glucose (FDG) is an established clinical PET tracer that can be used for qualitative and quantitative characterization of tissues with high energy demands [14, 15]. Like glucose, it is taken up from the blood stream by glucose transporters and phosphorylated by hexokinase once it is internalized. FDG is finally trapped and accumulates in the cytosol because it is not amenable to the subsequent glycolytic enzymes [16]. Currently, FDG-PET is an established method for staging in clinical oncology and it is widely used on PET/CT scanners that deliver anatomical localization at the same time [17]. However, it requires complementary approaches to better characterize malignant tissues, because FDG uptake is an indirect measure of the Warburg effect. Furthermore, it cannot discriminate between tumors and tissues that consume high amounts of glucose on a regular basis like in the brain, heart or during inflammatory processes [13, 18].

Magnetic resonance spectroscopic imaging (MRSI) has classically been used to study biochemical processes non-invasively, although it suffers from a low sensitivity and requires long scan times [19]. The invention of hyperpolarization (HP) techniques has shifted these limits, allowing signal enhancements of ^{13}C-labelled metabolites by more than five orders of magnitude [20]. However, hyperpolarized signals decay with the spin-lattice relaxation time (T_1) which is on the order of a few tens of seconds, limiting the time available for signal acquisition and requiring fast signal acquisition. Furthermore, supra-physiologic concentrations of ^{13}C-metabolites are administered to achieve analyzable *in vivo* spectra in pre-clinical and clinical [21] studies. In fact, this could potentially bias the quantification of metabolic parameters, but Serrao et al. have recently shown that exchange rates are not significantly altered by high metabolite concentrations in the blood stream [22].

Hyperpolarized [1-^{13}C]pyruvate (pyruvate) is most often used *in vivo*, because of its key role in glucose metabolism, its fast metabolic conversion to lactate, its high achievable polarization level and a relatively long T_1 [10]. Tumors readily internalize and metabolize pyruvate to lactate by lactate dehydrogenase (LDH-A). The expression of LDH-A is upregulated in many tumors, which results in an increased pyruvate-to-lactate conversion [23] that can be quantified with MRSI [24].

So far, only a few sites worldwide attempted to assess the flux of glucose through the glycolytic

pathway either sequentially or simultaneously with FDG-PET and pyruvate imaging (HyperPET [25-28]). Witney et al. demonstrated a late treatment effect [29] and Menzel et al. [30] showed a qualitative correlation between both imaging modalities. Ravoori et al. recently detected an early treatment response with pyruvate that was not observed with PET/CT [31]. However, these studies indicate that sequential imaging of FDG uptake and pyruvate-to-lactate conversion with different modalities might not be ideal, because the metabolic status of an organism could change drastically during transport of animals, if the delay between the experiments is too long, or if anesthesia is interrupted.

Precise temporal and spatial correlation of complementary PET and MR data can inherently be achieved with PET/MR. However, it is a relatively expensive modality and not a standard technique in preclinical and clinical research. Although it has been shown that co-registration of sequentially acquired PET and MR images is feasible, for instance in brain [32], PET/MR is particularly useful for regions of low CT contrast. In addition, the ability to perform diffusion-weighted imaging could benefit data interpretation as variations of the cell density might lead to apparently decreased tracer uptake or conversion, affecting quantification of PET and MRSI data [33].

In this study, we established and validated a workflow at a clinical whole-body PET/MR for the multiparametric characterization of the glycolytic flux in a pre-clinical MAT-B-III breast cancer model. We analyzed the *in vivo* correlation of FDG uptake with pyruvate-to-lactate conversion and performed a longitudinal study with a group of tumor-bearing rats to study the effect of changing tumor cellularity on metabolic PET and MRSI data.

Methods

Chemicals

All chemicals were used as purchased without further purification. Cell culture media (RPMI-1640 and Mc Coy's) were obtained from ThermoFisher Scientific (Waltham, MA, USA) and medium supplies (fetal calf serum, penicillin/streptomycin mixture) from Biochrom/Merck (Berlin, Germany). [1-^{13}C]pyruvate, OX063 ((tris(8-carboxy-2,2,6,6-tetra-(hydroxyethyl)-benzo-[1,2-4,5]-bis-(1,3)-dithiole-4-yl)-methyl sodium salt) and gadolinium chelate (Dotarem) for hyperpolarization were respectively obtained from Cambridge Isotope Laboratories (Tewksbury, MA, USA), Oxford Instruments (Abingdon, United Kingdom) and Guerbet Laboratories Ltd. (Villepinte, France). Isoflurane was purchased from CP-Pharma (Burgdorf, Germany). Pentobarbital (Narcoren) was purchased from Merial (Lyon, France). Chemicals for the dynamic nuclear polarization (DNP) dissolution buffer were obtained from Sigma Aldrich (St. Louis, MO, USA). FDG was synthesized on site using a standard technique modified from the synthesis reported by Hamacher et al. [34] and with chemicals purchased from Sigma Aldrich (St. Louis, MO, USA).

Tumor model

Animal experiments were approved by the local governmental committee for animal protection and welfare (Tierschutzbehörde, Regierung von Oberbayern).

Subcutaneous tumors were induced at the right flank of eleven female Fischer344 rats (age = six weeks, average weight = 146 ± 10 g; Charles River, Wilmington, MA, USA) by implantation of 1×10^6 MAT-B-III 13762 breast cancer cells derived from mammary adenocarcinoma (ATCC, Manassas, VI, USA). For this purpose, cells were cultivated in RPMI-1640 medium supplied with 10% fetal calf serum, 1% penicillin and 1% streptomycin and re-suspended in 200 µL Mc Coy's 5A medium for implantation. A tumor growth curve can be found in **Figure S1**.

Study population

For quantitative validation of FDG uptake measured in a clinical PET/MR scanner, three animals were imaged eight days after tumor implantation in a small-animal PET/CT scanner (Inveon, Siemens Healthcare, Erlangen, Germany) after two hours of fasting. Approximately ten hours later, the same animals were imaged again after two hours of fasting in a clinical 3T PET/MR scanner (Biograph mMR, Siemens Healthcare, Erlangen, Germany). Furthermore, eight animals were measured in the clinical PET/MR scanner eight, ten and thirteen days after tumor implantation in a longitudinal study (fed ad libitum). One hyperpolarized [1-^{13}C]pyruvate measurement was excluded from analysis because of respiratory problems during tracer injection, one PET scan failed (see workflow) and one animal was sacrificed on day ten, because it met a study abortion criterion. In total, ten comparable FDG-PET, HP [1-^{13}C]pyruvate and DWI measurements for day eight, eight for day ten and six for day thirteen were used for analysis and clustered into three groups of similar *ADC* values.

PET/MR workflow

For PET/MR scans, animals under anesthesia (1-3% isoflurane) were placed right lateral and head first with the tumor in the middle of the isocenter of

the magnet and on top of the center of a flexible $^{1}H/^{13}C$ dual-tuned transmit-receive surface coil (Rapid Biomedical, Rimpar, Germany). PET scans were started with tail-vein injection of FDG.

During PET acquisition (**Figure 1A**), a magnetic resonance-based attenuation correction ultra-short echo time (MRAC UTE), a 3D T_1 magnetization-prepared rapid acquisition gradient echo (MPRAGE), a 3D T_2-weighted fluid-attenuated inversion recovery (FLAIR), an axial 2D T_1-weighted (FLASH) and an axial 2D T_2-weighted half Fourier acquisition single shot turbo spin echo (HASTE) sequence were acquired. Metabolic imaging using pyruvate was performed at the end of the PET scan (~70-90 min after PET start) using an axial 2D chemical shift imaging sequence (CSI). For diffusion-weighted imaging, a 2D axial spin-echo, echo-planar imaging (EPI) sequence was applied. DWI was started after the PET scan was finished, because the sequence attempted to move the slice position in the isocenter of the bed, which interfered with PET acquisition. All 2D sequences were positioned in the same axial center of the tumors. Acquisition parameters of the proton MRI sequences are summarized in the supplement (**Table S1**). During PET/MR acquisition, blood oxygenation (Expression MR Patient Monitor, Invivo, Gainesville, FL, USA) and breathing rate (ECG Trigger Unit, Rapid Biomedical, Rimpar, Germany) were continuously monitored. With exception of one animal that stopped breathing (for about 60 s and then resumed breathing) after injection of pyruvate, breathing (50 ± 13 min^{-1}) and blood oxygen saturation (93 ± 6%) did not show any abnormalities during all performed experiments. Blood glucose (c_{Glc}) and blood lactate (c_{lac}) were determined before each measurement (Accutrend Plus, Roche, Basel, Switzerland). The average time of animals under anesthesia was 155 ± 27 min.

Tumor region-of-interest (ROI) definition

Quantification of metabolic and cellular parameters was performed for whole tumor ROIs. Detailed information will be given in the respective image analysis sections. The threshold for the region grower for PET analysis was chosen to cover the whole tumor in three dimensions including areas of lower FDG uptake. The acquisition slices of ^{13}C-images were oriented in the axial direction with the slices being in the middle of the tumors and having a slice thickness of 13 mm to cover the tumor in the axial direction. ROIs for ^{13}C-analysis were defined for the whole tumor in T_2-weighted images overlaid on ^{13}C-images. For diffusion-weighted imaging, three images (per *b*-value) with a slice thickness of 3 mm and a distance of 2 mm (total volume: 13 mm) between the slices were acquired to cover the same tumor volume as was measured with ^{13}C-CSI. For histology, four slices per tumor were analyzed with a total distance of 7-10 mm between the two slice pairs.

PET/CT acquisition and reconstruction

FDG-PET scans in the small-animal PET/CT were started with a tail-vein injection of FDG (11.5 ± 0.6 MBq). Three-dimensional PET data were acquired in list mode for 60 min followed by a CT-acquisition (low dose, 120 projections, 200 ms exposure time, 80 kVp (peak kilovoltage) x-ray voltage, 500 µA anode current at 220° rotation). Images were reconstructed in 12×10 s, 6×30 s, and 11×300 s frames using an ordered-subsets expectation-maximization 3D algorithm with 2 iterations and 16 subsets, followed by 18 maximum-a-posteriori iterations (recommended parameters from manufacturer), without

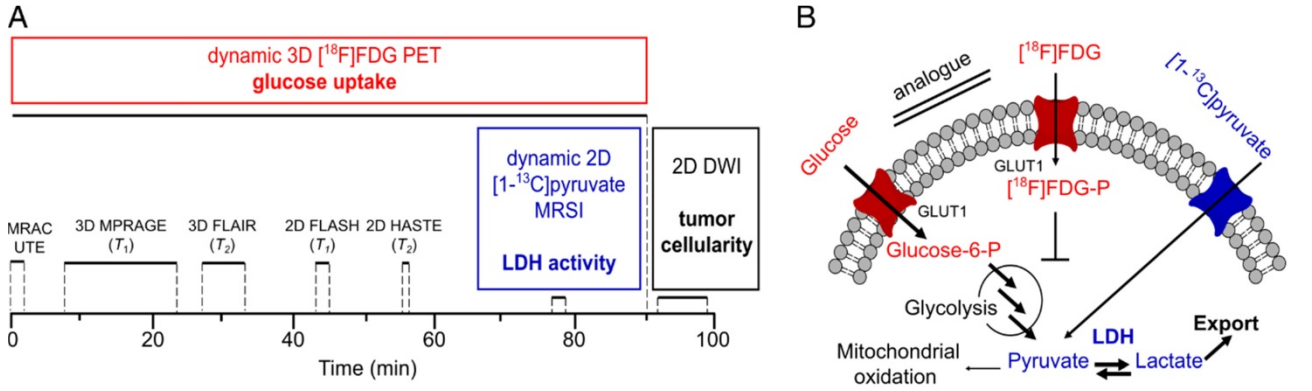

Figure 1. Multimodal imaging workflow (A) and addressed metabolic pathways (B). Dynamic 90 min PET acquisition was started with tail-vein injection of [^{18}F]FDG. Simultaneously, magnetic resonance-based attenuation correction ultra-short echo time (MRAC UTE), 3D and 2D T_1- and T_2-weighted proton MRI for determination of tumor localization and slice positioning of ^{13}C and DWI acquisition were performed. Dynamic ^{13}C-MRSI was measured after injection of HP pyruvate at the end of the PET scan (70-90 min after FDG injection). DWI was performed after PET acquisition. Metabolic parameters (glucose uptake and LDH activity) and structural parameters (tumor cellularity) that were addressed with PET, MRSI and DWI are given in bold. Acquisition times are indicated with black solid lines. Acquisition parameters for proton MRI can be found in the supplement (**Table S1**). Metabolic pathways (B) that were addressed with FDG-PET and ^{13}C-MRSI are colored in red and blue, respectively. Note that arrows with bigger fonts indicate an increased metabolic flux as observable for various tumors.

attenuation or scatter correction. The final image matrix was 128×128 pixels, 159 axial slices and a pixel size of 0.77×0.77×0.80 mm^3. The CT images were reconstructed with a modified Feldkamp algorithm yielding image matrices of 256×256 pixels, 384 axial slices and a pixel size of 0.17×0.17×0.17 mm^3.

PET/MR acquisition and reconstruction

3D FDG-PET data were acquired in list mode for 90 min after tail-vein injection of FDG (10.5 ± 2.1 MBq). Images were reconstructed with the same framing as described for PET/CT, using a fully iterative 3D OSEM (ordered subset expectation maximization) algorithm (3 iterations and 21 subsets as recommended by the manufacturer) with an ultra-short echo time magnetic resonance imaging-based attenuation correction (MRAC UTE). The final PET image matrix contained 344×344 pixels, 127 axial slices, and a voxel size of 1.04×1.04×2.03 mm^3 resulting in a FOV of 359×359×258 mm^3.

PET image analysis

PET analysis was performed in Matlab (The MathWorks, Natick, MA, USA). Tumor ROIs were semi-automatically segmented using a region grower algorithm with the initial seed manually selected. We calculated the standard uptake value (*SUV*) in the tumor ROI by normalizing the mean activity concentration in the ROI by the injected dose and the animal weight. All voxels, in which we measured an FDG activity greater than half of the maximum *SUV* (SUV_{max}) were appended to the ROI by the region grower (SUV_{mean}, with $SUV > 0.5 \times SUV_{max}$). The threshold was chosen in order to cover the whole tumor including areas of lower FDG uptake. All SUV values were measured on a 5 min frame 47 min post injection.

In addition, we calculated the total volume of voxels with $SUV_{mean} > 0.5 \times SUV_{max}$ which is defined as the tumor metabolic volume (*TMV*). The product of the SUV_{mean} and the *TMV* is the total lesion glycolysis (*TLG*). Both *TMV* and *TLG* are a measure of the metabolic burden [35, 36].

For PET Patlak [37] analysis, image-derived input functions (IDIFs) were segmented semi-automatically with a threshold of $0.7 \times SUV_{max}$ in the inferior vena cava in coronal images obtained from PET/CT and PET/MR. The average ROI size was 21 ± 10 mm^3. Tumor time-activity curves were fitted to a Patlak kinetic model (fit intervals: 10 min to 40 min) yielding the composite rate constant K_i ($K_1 \times k_3/(k_2+k_3)$), with k_1 being the primary tracer uptake rate from blood to free tracer in tissue, k_2 the tissue clearance rate and k_3 the rate of exchange between free and trapped tracer in tissue. The rate of tumor glucose uptake (*MRGlu*) was calculated as $K_i \times (c_{Glc}/LC)$, with *LC* being the lumped constant equaling 0.60 [30]. For PET/MR longitudinal data, K_i and *MRGlu* values were divided by a correction factor f = 2.7 that was obtained from the comparison of PET/CT and PET/MR data. More detailed information for Patlak analysis can be found in the supplement (**Section S2** and **S3**).

Hyperpolarization of pyruvate

For the HP process, 14 M [1-^{13}C]pyruvate (36.7 ± 1.9 mg) supplemented with 15 mM OX063 trityl radical and 1 mM Dotarem were polarized with a HyperSense (Oxford Instruments, Abingdon, United Kingdom) for ~30 min at 1.2 K using a microwave frequency of 94.155 GHz and 100 mW power. The sample was dissolved in a solution pressurized to 10 bar and heated to 180 °C containing 4.5 ± 0.3 mL 100 mM phosphate buffered saline (PBS) supplemented with 100 mM sodium hydroxide (NaOH) and 0.1 g/L sodium ethylenediaminetetraacetic acid (EDTA). Finally, the solution for injection contained an average pyruvate concentration of 90.3 ± 3.9 mM at pH 7.6 ± 0.2. The polarization level was about 38% (measured at B_0 = 1 T, Spinsolve Carbon, Magritek, Aachen, Germany) [38]. The hyperpolarized solution was rapidly transferred to the clinical PET/MR scanner and injected 21.7 ± 2.1 s after dissolution.

^{13}C-MRSI

The excitation profile of the ^{1}H/^{13}C surface coil was measured as shown in **Figure S4**. Prior to the *in vivo* experiments, the ^{13}C-resonance frequency was determined and a calibration of the B_1-field was performed using a 5 mL model solution containing 2.2 M [1-^{13}C]lactate (lactate), 5 mM Dotarem and 0.1% sodium azide. The ^{13}C-transmit frequency was set to the center between lactate and pyruvate. CSI was started at the same time as the injection of 1.0 ± 0.1 mL of hyperpolarized pyruvate and injection took 18.0 ± 5.1 s.

A slice-selective, 2D phase-encoded CSI sequence was applied with the following parameters: 3 kHz spectral bandwidth; 512 acquisition points; 5.9 Hz spectral resolution; 8×8 matrix size; 13 mm slice thickness; 8 cm FOV; 15° flip angle; 200 ms repetition time; 29 excitations; 5.8 s scan time per slice; 20 consecutive measurements/scan; 118 s total acquisition time, 10×10×13 mm^3 nominal voxel size. The k-space was sampled in elliptic order from the center on outwards.

For qualitative comparison of PET and ^{13}C-images, a CSI image with a separate animal that was not used for quantitative analysis was measured using a matrix size of 16×16 and nominal resolution of

0.5×0.5×13 mm³. Number of excitations and scan time were 128 and 28 s respectively. All other acquisition parameters were not changed.

^{13}C-Image analysis

Images were reconstructed as described previously (Matlab, The MathWorks, Natick, MA, USA) [39]. The data were zero-filled by a factor of four in both k-space space dimensions and by a factor of two in the temporal dimension prior to Fourier transformation. In the spectrum of each voxel and for each time step, the resonances of lactate and pyruvate were quantified by integration.

The mean of the integrals of the pyruvate and the lactate signals were determined for whole tumor ROIs. The ROIs were defined from axial T_2-weighted images overlaid on the ^{13}C-images. Mean signals were then fitted with a two-site-exchange model as follows [10]:

$$\frac{dM_{lac}(t)}{dt} = +k_{pl} \cdot M_{pyr}(t) - k_{lp} \cdot M_{lac}(t) - \rho_{lac}(M_{lac}(t) - \lim_{t\to\infty} M_{lac}(t)) \quad (1)$$

$$\frac{dM_{pyr}(t)}{dt} = -k_{pl} \cdot M_{pyr}(t) + k_{lp} \cdot M_{lac(t)} - \rho_{pyr}(M_{pyr}(t) - \lim_{t\to\infty} M_{pyr}(t)) \quad (2)$$

M_{lac} and M_{pyr} are the lactate and pyruvate z-magnetizations, k_{pl} and k_{lp} are the apparent rate constants for the pyruvate-to-lactate exchange and the reverse reaction. ρ_{pyr} and ρ_{lac} are the effective decay rates of the pyruvate and the lactate signal including T_1 relaxation and radiofrequency (RF) excitation. If the thermal signals at $\lim_{t\to\infty}(t)$ are neglected, the contributions from backward conversions, RF excitation and T_1-relaxation can be merged into effective relaxation rates $T_{1pyr,eff.}$ and $T_{1lac,eff.}$. Pyruvate data were fitted piecewise according to **Equation 3**:

$$M_{pyr}(t) = \begin{cases} \frac{r_{inj.}}{T_{1pyr,eff}}(1 - e^{-T_{1pyr,eff}\cdot(t-t_{arr.})} & t_{arr} \le t \le t_{max,pyr} - 5.9s \\ M_{pyr,max}\, e^{-T_{1pyr,eff}\cdot(t-(t_{max,pyr}+5.9s))} & t \ge t_{max,pyr} + 5.9s \end{cases} \quad (3)$$

where $r_{inj.}$ is the rate of injection, $t_{arr.}$ is the time of substrate arrival and $t_{max,pyr}$ is the time at the observed maximum of pyruvate.

We found that fitting of the lactate signal with the following differential equation was more reliable than using the input function parameters obtained by the pyruvate fit. This was mainly due to the fact that the sampling rate of ^{13}C-data was not high enough to accurately determine the actual $t_{max,pyr}$. For discrete values, the simplified differential **Equation 4** can be expressed as matrix equation for k_{pl} and $T_{1lac,eff.}$

$$dM_{lac}/\mathrm{d}t = k_{pl} \cdot M_{pyr}(t) - T_{1lac,eff} \cdot M_{lac}(t) \quad (4)$$

and solved using the Moore-Penrose pseudoinverse.

Furthermore we calculated the kinetic value from the area under the curves (*AUC* ratios) according to the model-free approach of Hill et al. [40] in **Equation 5**:

$$AUC\ ratios = \frac{\sum_{n=1}^{20} \overline{I(lactate_{tumor})}}{\sum_{n=1}^{20} \overline{I(pyruvate_{tumor})}} \quad (5)$$

with $I(lactate)_{tumor}$ and $I(pyruvate)_{tumor}$ being the summed mean lactate and pyruvate nuclear magnetic resonance (NMR) integrals observed in the same tumor ROIs as mentioned above.

Additionally to analysis of tumor ROIs, we analyzed mean pyruvate and lactate integrals measured in the whole axial CSI slice, which is similar to a slice-selective excitation approach yielding $k_{pl,\mathrm{slice}}$ and AUC ratios$_{\mathrm{slice}}$. This avoids errors of manual ROI determination but instead includes pyruvate and lactate signals from regions outside of the tumor.

Diffusion-weighted image analysis

We performed experiments with an ice-water phantom [41] to show reproducibility and validation for *ADC* quantification. Detailed information is given in the **Supplement S5**. *In vitro* and *in vivo* tumor apparent diffusion coefficients (*ADC*) were calculated from the image intensities (*S*) according to the Stejskal-Tanner **Equation 6** [42]:

$$S = S_0 \cdot e^{(-b \cdot ADC)} \quad (6)$$

with S_0 being the image signal intensity without diffusion-weighting and b being the diffusion-weighting factor.

Calculations were performed using least squares fitting and calculations resulted in pixelwise *ADC*-maps (MATLAB, MathWorks, Natik, MA, USA). The *ADC* values were obtained at first by averaging the signal intensities in the manually segmented ROI and subsequently calculating the *ADC* value. The workflow was performed for three slices per animal to cover the whole tumor in the axial direction. Finally, a weighted mean of three slice-specific *ADC* values per animal was determined [43, 44]. A representative series of T_2-weighted images, diffusion-weighted images and *ADC* fits are shown in the supplement (**Figure S5**).

Histology

Seven animals from terminal experiments were sacrificed with an excess of pentobarbital (n = 1 and n = 6, respectively, ten and thirteen days after tumor implantation). One animal was left out for analysis, because the PET scan failed as described in the workflow section. Tumors and adjacent tissue were removed, marked according to their spatial orientation and divided in two halves that were subsequently fixed in 10% neutral-buffered formalin solution for 48 h, dehydrated under standard conditions (Leica ASP300S, Wetzlar, Germany) and embedded in paraffin. Each half was flattened and from each half two 2 um-thin sections, separated by 200 µm and with a distance of 7-10 mm to the slices from the other tumor half (distance of the outer slices) were prepared with a rotary microtome (HM355S, ThermoFisher Scientific, Waltham, MA, USA), collected and subjected to histological analysis. Hematoxylin-Eosin (H.-E.) staining was performed on deparaffinized sections with Eosin and Mayer's Haemalaun according to a standard protocol.

The percentage as well as the pattern of necrosis (i.e., large central necrosis vs. multifocal small areas of necrosis) covering the tumor area were evaluated by two experienced pathologists. Representative H.-E. stained images are given in the supplement (**Figure S6**). Percentages of necrosis are given as mean (± standard deviation) values calculated for all slices (**Figure S7**).

Measurement of distance between tumor and blood vessel

The distance between the vena cava and the center of mass of the tumors ($d_{t\text{-}v}$) was defined in T_2-weighted images (RadiAnt Dicom Viewer, Medixant, Poznan, Poland).

Statistical analysis

All data are represented as mean values and standard deviations (*std*). Correlations for all quantitative parameters were calculated with a two-sided *t*-test yielding the Pearson product-moment coefficient (R) using GraphPad Prism (GraphPad Software, Inc., La Jolla, CA, USA). Longitudinal data were analyzed with an unpaired two-sided *t*-test. Values of < 0.3, 0.3-0.5 and 0.5-1.0 were considered as weak, moderate and strong correlations, respectively, according to the guidelines of Cohen [45] and as reported earlier [46]. The statistical significance levels are indicated by asterisks, *p < 0.05, **p < 0.01, ***p < 0.001, ****p < 0.0001.

Results

Validation of FDG uptake measured at a human PET/MR compared to a small-animal PET/CT

Tumor-time activity curves measured with pre-clinical PET/CT and clinical PET/MR are displayed in **Figure 2A-B**. The SUV_{max} values were 7.4 ± 1.2 and 7.5 ± 0.7 and the SUV_{mean} values were 4.9 ± 0.5 and 4.8 ± 0.6 for the PET/CT and PET/MR respectively, showing no significant difference (t = 47 min, **Figure 2C**). For kinetic analysis of FDG uptake, image-derived input functions (IDIFs) could reproducibly be measured in the inferior vena cava (see supplement, **Figure S2** [47]) rather than in the aorta where the IDIF was not quantifiable [48]. However, the area under the curve values of IDIFs (**Figure S3**) were smaller for IDIF measurements at the PET/MR (**Figure 2E**) compared to the PET/CT (**Figure 2D**). This caused an overestimation of PET/MR K_i values by a factor of f = 2.7 (**Figure 2F**).

Metabolic mapping of hyperpolarized pyruvate

HP pyruvate was readily observed in the vena cava in the first CSI images (t = 5.9 s) after tail-vein injection. Lactate was observed in the subsequent data sets. The maximum signals of pyruvate and lactate in the tumor were observed at 22 ± 4 s and 27 ± 4 s, respectively, after the start of the acquisition. Representative metabolic images of pyruvate and lactate at time t = 23.6 s from a dynamic time course are displayed in **Figure 3A** and **Figure 3D**, respectively. The signal of pyruvate was about five-fold higher in the vena cava than in the tumor and about ten-fold higher than the maximum lactate signal. Effective relaxation rates of pyruvate and lactate in tumor ROIs were $T_{1pyr,eff.}$ = 14.6 ± 2.0 s and $T_{1lac,eff.}$ = 9.8 ± 2.5 s (n = 24). Hyperpolarized lactate was mainly visible in tissues around the vena cava and the tumor. *AUC* ratios and k_{pl} indicated a higher LDH activity in the tumors (*AUC* ratios = 0.28 ± 0.06, k_{pl} = 0.029 ± 0.009 s^{-1}) than in tissues surrounding the vena cava (*AUC* ratios = 0.10 ± 0.01, k_{pl} = 0.015 ± 0.004 s^{-1}). The time course of pyruvate and lactate signals of a representative tumor and a non-tumor voxel are shown in **Figure 3B** and **Figure 3E**. Respective plots of the integrals of the dynamic NMR series are given in **Figure 3C** and **Figure 3F**. Tumor *AUC* ratios and k_{pl} values showed a strong positive correlation (R = 0.62, p = 0.0012), as reported in the literature [40].

We observed that partial volumes and point spread function [49] artifacts caused by both a high pyruvate blood signal and a low spatial resolution of ^{13}C-images influenced the tumor k_{pl} and *AUC*, especially in cases where the tumor was close to the

vessel. A positive correlation between the tumor k_{pl} and AUC ratios with the distance of the tumor ($d_{t\text{-}v}$) to the blood vessel illustrates this effect (R = 0.66, p = 0.0004 and R = 0.60, p = 0.0020, respectively, **Figure 4A-B**).

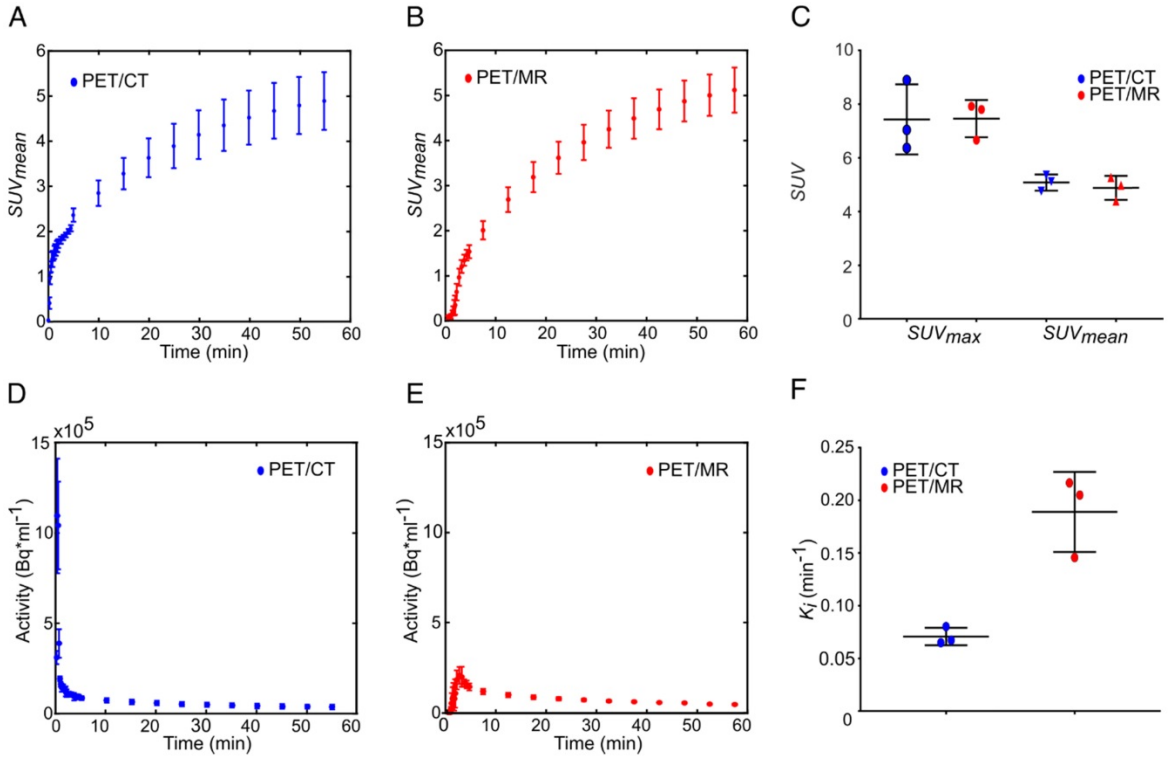

Figure 2. Comparison of the FDG uptake and Patlak analysis of subcutaneous MAT-B-III tumors measured with a pre-clinical PET/CT and a clinical PET/MR scanner. FDG uptake curves of subcutaneous tumors obtained from the **(A)** PET/CT (blue) and the **(B)** PET/MR (red). **(C)** The comparison of SUV_{max} and SUV_{mean} does not show a significant difference between the two systems. **(D-E)** are image-derived input functions (IDIFs) used for Patlak analysis measured in the inferior vena cava for PET/CT and the PET/MR images, respectively. **(F)** shows that the K_i values obtained from PET/MR measurements are overestimated by a factor of 2.7 compared to values obtained with the PET/CT. Note that equal thresholds for the region grower algorithm were used to obtain quantitative PET/CT and PET/MR data (tumor: 0.5×SUV_{max}, input function: 0.7×SUV_{max}).

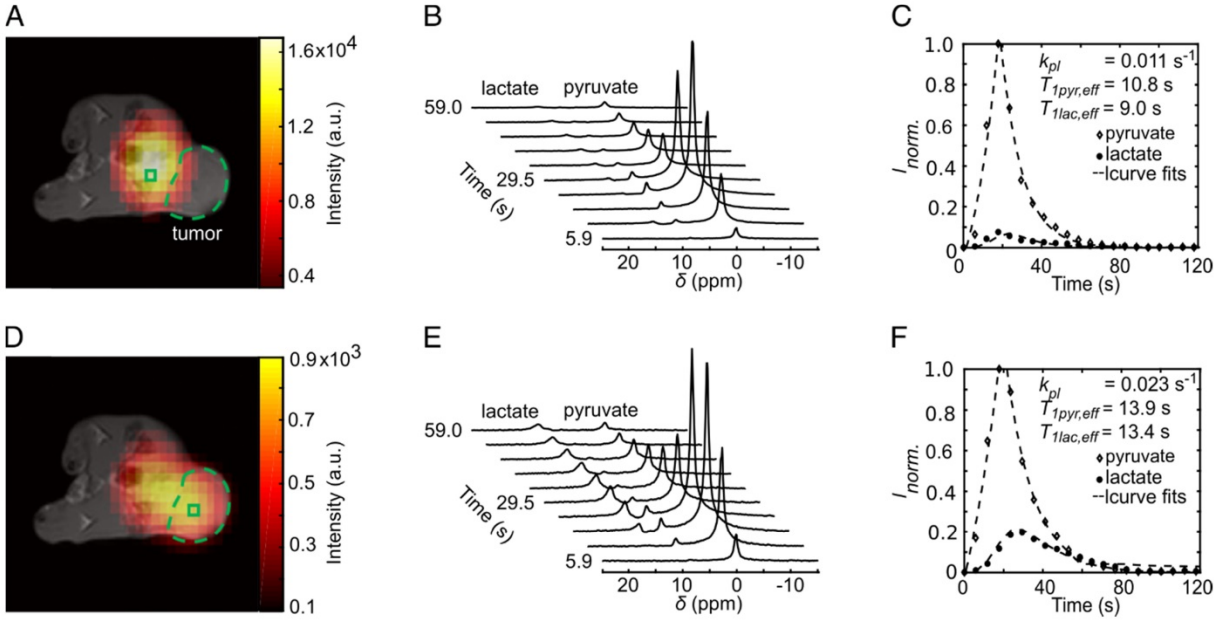

Figure 3. Dynamic metabolic mapping of the LDH activity of subcutaneous MAT-B-III tumors using hyperpolarized pyruvate. (A) Static image of hyperpolarized pyruvate at pyruvate maximum in tissues surrounding the vena cava overlaid on an axial T_1-weighted image. A non-tumor voxel is indicated with the green box, the tumor is delineated with the green dashed line. **(B)** Stacked plot of the first ten dynamic ^{13}C-spectra of a non-tumor voxel from (A). **(C)** Dynamic series of pyruvate and lactate NMR signal integrals from (B) and normalized to the maximum integral of pyruvate ($I_{norm.}$). Curve fits are given with dashed lines. **(D)** Static image of hyperpolarized lactate at lactate maximum overlaid on an axial T_1-weighted image. **(E)** Stacked plot of the first ten NMR spectra from a representative tumor voxel (green box in (D)). **(F)** Dynamic series of pyruvate and lactate NMR signal integrals of the tumor ROI and normalized to the maximum integral of pyruvate. Curve fits are given with dashed lines. Note that the pyruvate signal was about a factor of ten higher than that of lactate.

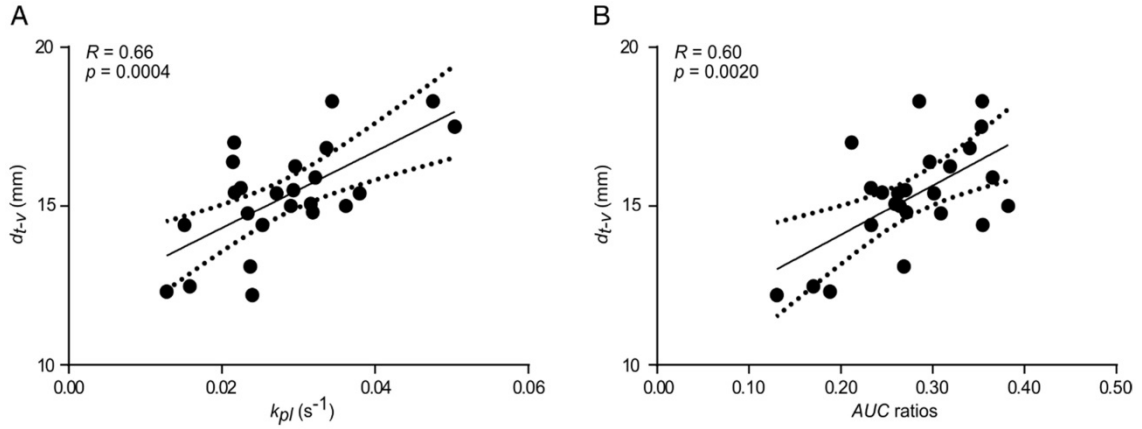

Figure 4. Correlation between k_{pl} (A) and *AUC* ratios (B) with distance between the major blood vessel and the center of MAT-B-III tumors ($d_{t\text{-}v}$). Best fit (solid line) and 95% confidence bands (dashed lines).

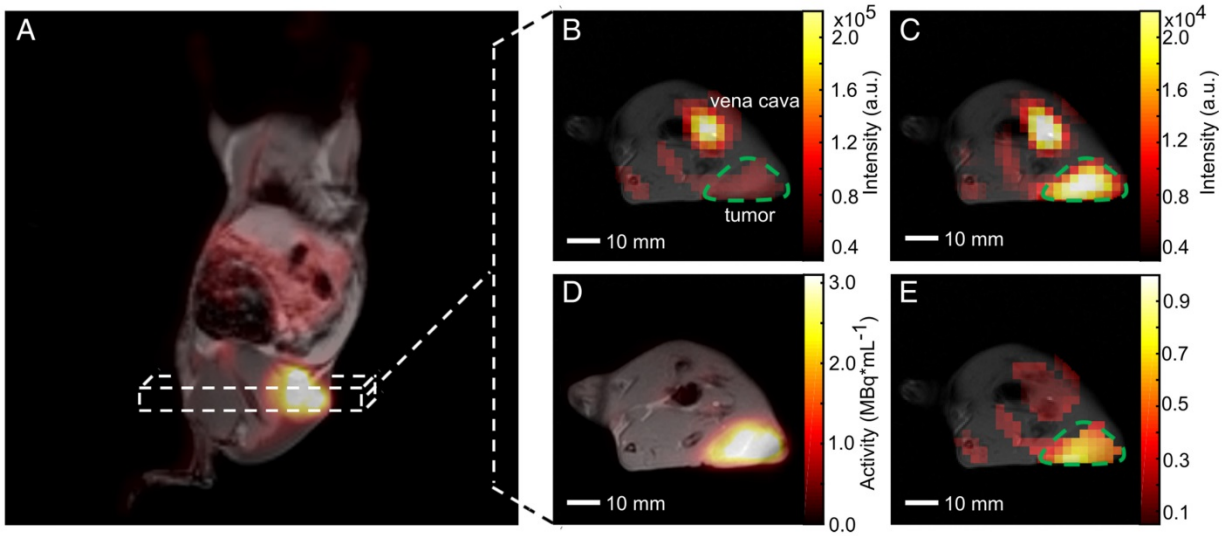

Figure 5. Qualitative comparison of simultaneously imaged FDG uptake and pyruvate-to-lactate exchange in MAT-B-III tumor-bearing rats. (A) Coronal slice of a late frame PET image overlaid on the respective slices of an MPRAGE image. Static axial images of pyruvate **(B)**, lactate **(C)** and FDG **(D)** in the same orientation. **(E)** is the ratio of (C) and (B) showing a higher lactate to pyruvate ratio in the tumor than observed in the surrounding tissue, which correlates well with the high FDG uptake shown in (D). Note that for CSI images, only pixels with a signal > 20% of the maximum signal of hyperpolarized pyruvate and lactate are displayed, respectively. Note further that the pyruvate signal is about a factor of ten higher than the lactate signal and that the nominal resolution of ^{13}C-images was two-fold higher than the resolution used for quantitative analysis.

Qualitative comparison of PET and HP-MRSI

Our PET/MR setup enabled the acquisition of three-dimensional T_1- and T_2-weighted proton images of whole animals (except the head) with a resolution below one cubic millimeter (**Table S1**). This allowed an accurate tumor delineation in the axial direction, which facilitated the positioning of 2D proton images that were used for anatomical referencing of MRSI and DWI. Quantification of pyruvate-to-lactate exchange was based on tumor ROI definition on ^{13}C-images overlaid with 2D T_2-weighted proton images. Two- and three-dimensional T_1-weighted proton images were used for visualization of inherently co-registered PET or MRSI data as shown in **Figure 5**.

A coronal (from 3D T_1-weighted images) and an axial static late frame FDG image (t = 55 min) show high FDG uptake in tumors (**Figure 5A** and **Figure 5D**). Representative static metabolic images of hyperpolarized pyruvate and lactate are displayed in **Figure 5B** and **Figure 5C** revealing pyruvate uptake and conversion to lactate in the same region as given in **Figure 5D**. **Figure 5E** displays the ratio of lactate-to-pyruvate and indicates a high pyruvate-to-lactate exchange in the tumor region, which qualitatively correlates well with a high FDG uptake (**Figure 5D**).

Quantitative comparison of PET and DWI and HP MRSI data

We measured 24 multimodal longitudinal PET/MR data sets to investigate the correlation between FDG uptake and pyruvate-to-lactate exchange and the effect of tumor cellularity on metabolic data. However, it has to be noted again that

ROIs for PET, DWI and MRSI analysis did not exactly correlate in space, as mentioned in the methods.

ADC values significantly increased with tumor growth (**Figure S8A**) due to increasing necrosis. This was verified by histological analysis (**Figure S7**) that showed a positive but not significant correlation between *ADC* and percentage of necrosis for the terminal samples (R = 0.46, p = 0.2150, n = 7). Metabolic data showed a negative correlation with increasing necrosis without significance (SUV_{mean}: R = -0.46, p = 0.2960, K_i: R = -0.68, p = 0.0916), whereas only a very weak trend was observable for ^{13}C-data (k_{pl}: R = -0.23, p = 0.6147). Comprehensive plots are shown in **Figure S7**. Note, that only small amounts of granulation tissue in the necrotic parts and immune cell infiltration were observed.

Based on these observations, we clustered quantitative ^{13}C- and PET data into three groups of low, medium and high *ADC* values: (0.57 ± 0.04)×10^{-3} mm^{2}s^{-1}, (0.85 ± 0.09)×10^{-3} mm^{2}s^{-1} and (1.22 ± 0.10)×10^{-3} mm^{2}s^{-1} (with n = 13, n = 7 and n = 4, respectively). We then analyzed the correlation of quantitative PET and ^{13}C-data of the low *ADC* group in order to exclude partial volume effects that affect metabolic data caused by a varying tumor cellularity (**Figure 6**).

Tumor k_{pl} exhibited a significant positive correlation with SUV_{mean} (R = 0.59, p = 0.0352, **Figure 6A**) and K_i (R = 0.57, p = 0.0399, **Figure 6C**). A similar but not significant trend was observed with SUV_{max} (R = 0.51, p = 0.0761, **Figure 6B**) and no correlation was seen with *MRGlu* (R = 0.05, p = 0.8636, **Figure 6D**). Tumor *AUC* ratios significantly correlated with SUV_{mean} (R = 0.59, p = 0.0326, **Figure 6E**), SUV_{max} (R = 0.55, p = 0.0498, **Figure 6F**) and K_i (R = 0.68, p = 0.0103, **Figure 6G**), but not with *MRGlu* (R = 0.36, p = 0.2245, **Figure 6H**). Slice-selective k_{pl} and *AUC* ratios, excluding errors from manual tumor ROI definition, also showed a positive correlation with quantitative PET data: $k_{pl,\,slice}$ with SUV_{mean}: R = 0.56, p = 0.0481 and with K_i: R = 0.65, p = 0.0158; *AUC* ratios$_{slice}$ with K_i: R = 0.70, p = 0.0079 and with *MRGlu*: R = 0.81, p = 0.0008. A comprehensive correlation matrix for tumors with a similar *ADC* can be found in the supplement (**Table S2**).

Longitudinal PET data showed a significant inverse correlation with *ADC*, while a similar but not significant trend was observed for k_{pl}. No correlation or trend was observed between *AUC* ratios and *ADC*. Representative correlation plots of SUV_{mean} and k_{pl} with *ADC* are given in **Figure 7**. A comprehensive matrix of Pearson correlation coefficients for longitudinal data can be found in **Table 1**, excluding slice-selective-like ^{13}C-data analysis (see **Table S3**).

Overall, k_{pl} (**Figure S8C**) and PET uptake (SUV_{mean}, SUV_{max}, K_i and *MRGlu*) apparently decreased (**Figure S8D-G**) for bigger tumors. With tumor growth, the tumor metabolic volumes (*TMW*, **Figure S8H**) and the total lesion glycolysis (*TLG*, **Figure S8I**) increased and showed a strong correlation with *ADC* values (R = 0.81, p < 0.0001; R = 0.73, p < 0.0001, respectively, **Table 1**) and with the blood lactate concentration (R = 0.60, p = 0.0020; R = 0.51, p = 0.0118, respectively; **Table 1** and **Figure S8J**). In addition, we detected an inverse correlation of PET SUV_{mean} /SUV_{max} and k_{pl} with blood lactate concentration (R = -0.52, p = 0.0099; R = -0.48, p = 0.0172; R = -0.44, p = 0.0314; **Table 1**), which increases for animals with bigger tumors. Blood glucose levels slightly decreased but without significance (**Figure S8 K**). *AUC* ratios did not change significantly and solely correlated with SUV_{mean} (R = 0.41, p = 0.0484). Similar but not significant trends were observed for their correlations with SUV_{max}, K_i and *MRGlu* (R = 0.37, p = 0.0728; R = 0.37, p = 0.0747; R = 0.25, p = 0.2374). For k_{pl}, we observed significant positive correlations with tumor SUV_{mean} /SUV_{max} (R = 0.67, p = 0.0004; R = 0.61, p = 0.0014) and K_i (R = 0.65, p = 0.0006), which was not detected for *MRGlu* (R = 0.34, p = 0.1081).

Table 1. Pearson correlation coefficients for [^{18}F]FDG PET, [1-^{13}C]pyruvate CSI, DWI

	SUV_{mean}	SUV_{max}	K_i	*MRGlu*	k_{pl}	*AUC rat*	$d_{t\text{-}v}$	*TMW*	*TLG*	*ADC*	c_{lac}	c_{glc}
SUV_{mean}	1											
SUV_{max}	0.99****	1										
K_i	0.68***	0.60**	1									
MRGlu	0.65***	0.58**	0.94****	1								
k_{pl}	0.67***	0.61**	0.65***	0.34$^{n.s.}$	1							
AUC rat	0.41*	0.37$^{n.s.}$	0.37$^{n.s.}$	0.25$^{n.s.}$	0.62**	1						
$d_{t\text{-}v}$	0.25$^{n.s.}$	0.19$^{n.s.}$	0.45$^{*.}$	-0.07$^{n.s.}$	0.66***	0.60**	1					
TMW	-0.49*	-0.49*	-0.37$^{n.s}$	-0.34$^{n.s.}$	-0.33$^{n.s.}$	0.21$^{n.s.}$	0.22$^{n.s.}$	1				
TLG	-0.29$^{n.s.}$	-0.29$^{n.s.}$	-0.27$^{n.s.}$	-0.24$^{n.s.}$	-0.21$^{n.s.}$	0.38$^{n.s.}$	0.26$^{n.s.}$	0.95****	1			
ADC	-0.45*	-0.46*	-0.36$^{n.s}$	-0.37$^{n.s.}$	-0.38$^{n.s.}$	0.03$^{n.s.}$	0.38$^{n.s.}$	0.81****	0.73****	1		
c_{lac}	-0.52**	-0.48*	-0.30$^{n.s.}$	-0.19$^{n.s.}$	-0.44*	-0.13$^{n.s.}$	0.08$^{n.s.}$	0.60**	0.51*	0.35$^{n.s.}$	1	
c_{glc}	0.14$^{n.s}$	0.13$^{n.s.}$	0.17$^{n.s.}$	0.49**	-0.17$^{n.s.}$	0.11$^{n.s.}$	-0.20$^{n.s.}$	0.02$^{n.s.}$	0.06$^{n.s.}$	-0.11$^{n.s.}$	0.17$^{n.s.}$	1

$^{*}p < 0.05$, $^{**}p < 0.01$, $^{***}p < 0.001$, $^{****}p < 0.0001$

ADC: apparent diffusion coefficient; *AUC* rat: *AUC* ratios; c_{glc}: blood glucose concentration; c_{lac}: blood lactate concentration; $d_{t\text{-}v}$: distance of tumor to central blood vessel; K_i: composite rate constant; k_{pl}: pyruvate-to-lactate exchange rate; *MRGlu*: metabolic rate of glucose utilization; n.s.: not significant; SUV_{max}: maximum standard uptake value; SUV_{mean}: mean standard uptake value; *TLG*: total lesion glycolysis, *TMW*: tumor metabolic volume.

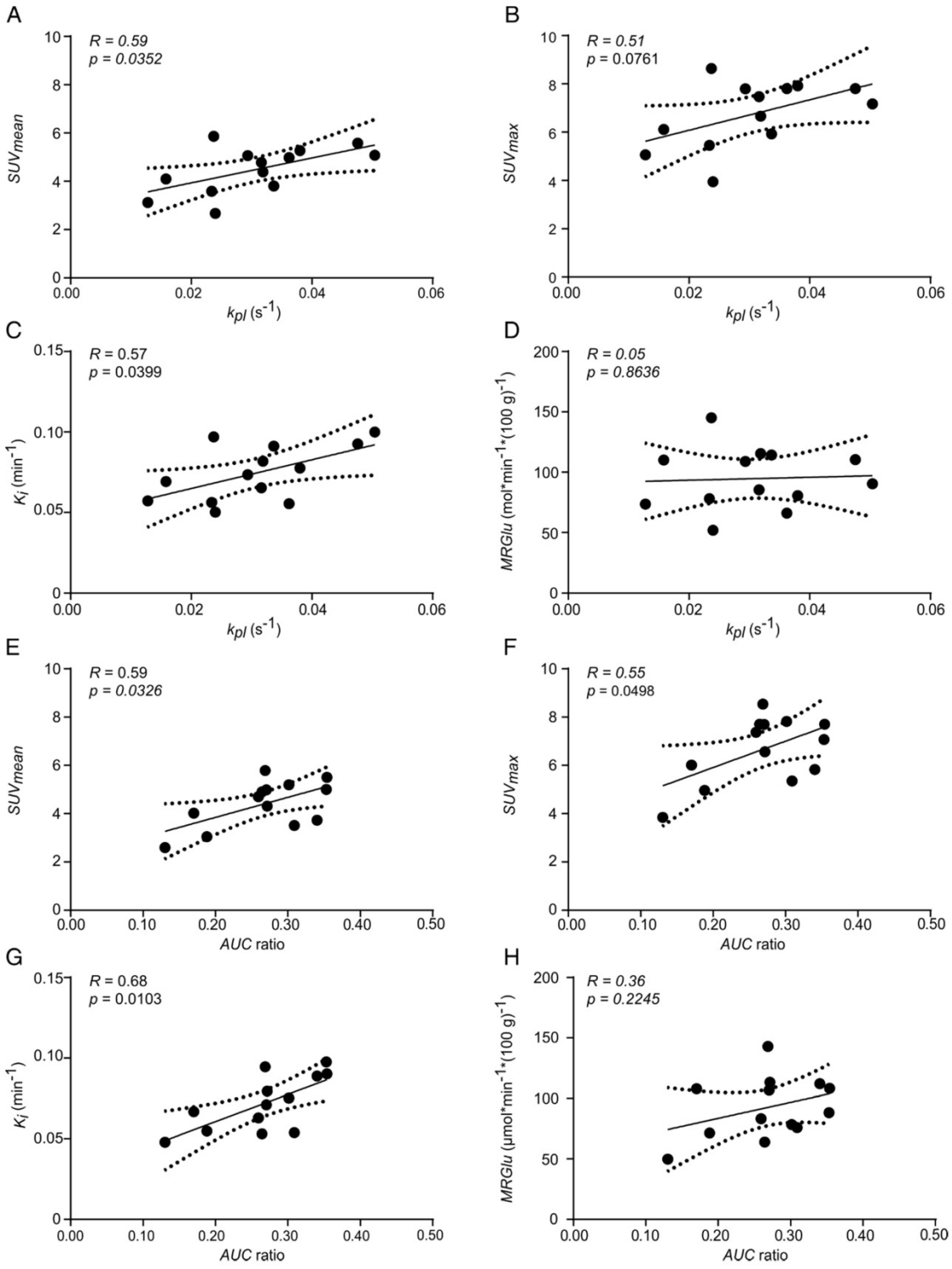

Figure 6. Correlation plots of FDG uptake and hyperpolarized pyruvate CSI data of tumors with similar *ADC* values. Correlation of k_{pl} with **(A)** SUV_{mean}, **(B)** SUV_{max}, **(C)** K_i and **(D)** *MRGlu*. Correlation of *AUC* ratios with **(E)** SUV_{mean}, **(F)** SUV_{max}, **(G)** K_i and **(H)** *MRGlu*. Best fit (solid line) and 95% confidence bands (dashed lines). The mean *ADC* of analyzed tumors was (0.57 ± 0.04)×10^{-3} mm^{2}s^{-1} (n = 13).

Discussion

We established and validated a multimodal imaging workflow on a whole-body PET/MR scanner to characterize the Warburg effect in a pre-clinical tumor model in rats. Using this workflow, we addressed the glycolytic flux in tumors and analyzed the effect of tumor growth on longitudinal metabolic data. Our setup enables the acquisition of high-resolution anatomical images and the quantification of physiological and biochemical data with PET, MRSI and DWI in one scan session. Furthermore, it has potential for translation to large

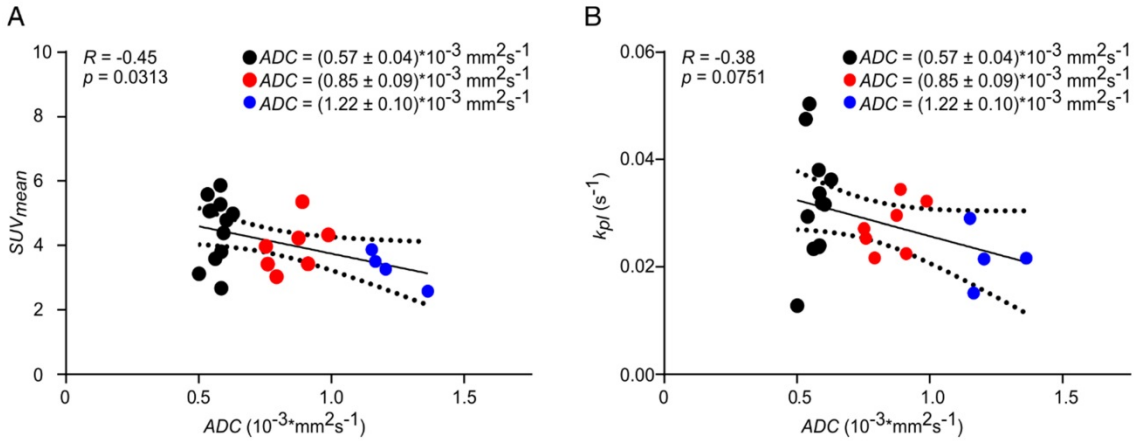

Figure 7. Correlation of SUV_{mean} (A) and k_{pl} (B) with *ADC*. Longitudinal data were clustered into three groups (black, red, blue) of different *ADC* values to analyze the effect of tumor cellularity on metabolic data. Best fit (solid line) and 95% confidence bands (dashed lines).

animal models [25, 26, 28] and into the clinic, where it could prove the oncological value of hybrid PET/MR.

FDG is an important tracer for diagnosis, staging and response to treatment monitoring of malignant tissues [17]. Comparative measurements with the gold-standard for pre-clinical imaging (PET/CT) showed that tumor *SUV*s (tumor size: >500 mm^3) can be measured reliably using a clinical system that has an isotropic spatial resolution of 4.3 mm [50]. However, quantification of FDG uptake could be biased due to false-positive results of glycolytic granulation tissue and infiltrating immune cells [51]. Histological analyses detected only a low proportion of fibroangioblastic granulation tissue consistent with a mesenchymal reaction to tumor implantation, whereas no distinct differences between animals were noticed. Furthermore, only scarce immune cell infiltration (mainly consisting of lymphocytes) surrounding the tumor tissue was observed and only single immune cells were present within the neoplasia (**Figure S6**).

In small structures like the inferior vena cava (~3 mm diameter for rats [52]), the activity recovery is biased due to partial volume effects, which leads to an overestimation of the composite rate constant (K_i). The spatial resolution of the PET/CT (<1.5 mm [53]) is about a factor of three higher than that of the PET/MR, allowing a better quantification of the input function and correction of the PET/MR data. However, for future studies we seek to approximate this correction factor more accurately either by measurements with dynamic contrast-enhanced (DCE) MRI [54] or by invasive arterial blood sampling [55]. Nevertheless, it should be noted that input functions could reproducibly be measured (**Figure S2**) in the inferior vena cava [47, 48] with a clinical PET/MR, enabling a quantification of tumor glucose consumption (*MRGlu*) even though values are biased.

Chemical shift imaging (CSI) is a reliable sequence to acquire spatially resolved spectroscopic data *in vivo*. However, CSI requires a single excitation for the acquisition of each position in the k-space for spatial information, and thus results in relatively long scan times and an ineffective use of HP magnetization. Nevertheless, we were able to perform time-resolved CSI measurements with a matrix size of 10×10×13 mm^3 and obtained time courses of pyruvate-to-lactate exchange that allowed a quantification of *in vivo* rate constants of LDH. However, due to the low image resolution, we defined whole tumor ROIs including necrotic areas for analysis. This caused partial volume effects likely yielding smaller apparent rate constants (k_{pl} and *AUC*). In addition, quantitative LDH measures (**Figure 4**) were further underestimated due to partial volumes and point spread function artifacts [49], in particular for the pyruvate signal in the vena cava, likewise caused by the low image resolution. Methods to partially compensate for such artifacts would for instance be the inclusion of an arterial [56] or image-derived input function for pyruvate. However, we found that due to the low data sampling rate, the latter approach was not as reliable as solving the differential equation (**Equation 4**) with the pseudoinverse of the matrix equation. At this point it should also be noted that a lower sensitivity of the ^{13}C-coil further away from its surface probably also impeded optimal quantification (**Figure S4**). In future, implementation of fast state-of-the-art imaging sequences like IDEAL spiral CSI [57], spectral-spatial EPI [58] or echo planar spectroscopic imaging (EPSI) [39] could be used to increase spatial resolution, which will improve the quantification of *in vivo* ^{13}C-data.

In the past, several studies sequentially measured FDG uptake and pyruvate-to-lactate

exchange on consecutive days [29]. Menzel et al. noticed that longer delays between experiments might change the glucose metabolism, obscuring the biological significance of metabolic information [30]. Simultaneously acquired FDG-PET and HP-pyruvate MRSI data for tumors with similar cell density herein demonstrated a positive qualitative (**Figure 5**) and quantitative (**Figure 6**) correlation between FDG uptake and LDH activity. However, metabolic images from different acquisitions were not precisely matched in space and correlations of quantitative data are probably still biased. In the future, this could be improved by an analysis of ROIs that are identical in space and dimension. Furthermore, provided that the spatial resolution of MRSI could be improved, inclusion of a voxel-wise [25] or histogram-based analysis could be beneficial to address tumor heterogeneity in greater depth [44].

Our workflow included diffusion-weighted imaging to address changes of tumor cellularity with tumor growth, because variations of tissue density and "tissue organization and extracellular space tortuosity" [44] can affect image-derived FDG uptake and pyruvate-to-lactate conversion. DWI is an emerging technique in oncology for diagnosis, monitoring and outcome prediction of malignancies. However, the diffusion encoding is inherently sensitive to motion and the imaging readout based on single-shot echo planar imaging (EPI) is prone to image distortions, as partially observed in our study (**Figure S5**). This could lead to quantification errors. We therefore performed comparative measurements with standardized phantoms, which revealed a good reproducibility of *ADC* measurements between different systems, yielding values in agreement with the literature (**Supplement S5**).

As *ADC*s significantly changed with tumor growth, we clustered longitudinal data in three groups of low, medium and high *ADC*. By minimizing the influence of variations in cell density on metabolic data, the correlation of FDG uptake (SUV_{mean} and K_i) and pyruvate-to-lactate exchange indicates that a major portion of consumed glucose is reduced via pyruvate to lactate for the low *ADC* group. Tumors use oxidative glycolysis to generate fast energy from glucose and fulfill their anabolic needs [13]. The excessive lactate production is crucial for invasion and immune evasion of tumors, facilitating their survival and metastasis [59]. A quantitative measure of the lactate production in tumors (k_{pl} or *AUC* ratios) is therefore valuable information that is complementary to FDG-PET and will potentially allow a more precise and patient-specific phenotyping.

Our setup enables the simultaneous quantification of FDG uptake, LDH activity and tumor cellularity to analyze the impact of tumor tissue density on metabolic data. In fact, negative correlations of longitudinal PET and DWI (**Table 1** and **Figure 7**) data showed that the measured FDG concentration (e.g., SUV_{mean} or K_i vs. *ADC*) decreases with decreasing tumor cellularity (**Figure S8**). This was validated by histology (**Figure S7**) and is in agreement with the literature [33, 60-62]. Similar effects were observed with ^{13}C-data (k_{pl}), but we assume that a rather imprecise quantification caused by a limited spatial resolution of our ^{13}C image obscured the significance. In addition, k_{pl} values appeared to reflect longitudinal averaging effects better than *AUC* ratios, where no trend was observed for the correlation with *ADC*.

With tumor growth, the overall tumor cellularity decreased while the absolute number of active tumor cells increased. This was indicated by increasing *TMW* and a strong positive correlation of the respective parameters (*ADC* and *TMW*). Thus, the absolute amount of FDG uptake (*TLG*) and lactate production in tumors both increased, which led to a progressive lactate acidification of animals. This was reflected by an increasing blood lactate concentration (c_{lac}) for animals with bigger tumors and its strong positive correlation with *TMW* and *TLG* [63].

Finally, longitudinal PET and ^{13}C-data also showed a positive correlation (k_{pl} with SUV_{mean}/SUV_{max} and K_i, *AUC* ratios with SUV_{mean}). Taking the results of the low *ADC* group and the correlations of the longitudinal data with *ADC* into account, we conclusively assume that this correlation is a combined effect of the Warburg effect and partial volume effects.

The simultaneous acquisition of high-resolution anatomical images, DWI, PET and hyperpolarized MRSI data is now possible with hybrid PET/MR in a clinical environment [25, 26, 28]. Better acquisition schemes for fMRI and MRSI and the growing number of approved PET tracers and hyperpolarized probes will further help to characterize tumor biology in greater depth.

Conclusions

We established and validated a multimodal imaging workflow for a clinical PET/MR scanner to simultaneously quantify glucose uptake, LDH activity and cell density in rodents with PET, hyperpolarized MRSI and DWI. Despite resolution limitations of dynamic ^{13}C-data, we demonstrated a good correspondence between high glucose uptake and elevated LDH activity in tumors of similar cellularity. This indicates that a major portion of glucose is

reduced to lactate in the analyzed tumor model. Longitudinal DWI data showed a decrease in cell density during tumor growth, which affected the quantification of both PET and MRSI data.

Our workflow includes a multiparametric and non-invasive tumor characterization that can possibly be applied to larger animal models with potential for clinical applications paving the way for tailored and patient-specific therapy approaches.

Abbreviations

2D: two-dimensional in space; 3D: three-dimensional in space; *ADC*: apparent diffusion coefficient; *AUC* ratio: areas under the curve ratio from tumor region-of-interest ^{13}C-analysis; *AUC* ratio$_{slice}$: areas under the curve ratio from slice-selective like ^{13}C-analysis; B_0: static magnetic field; B_1: radiofrequency excitation field; *b*-value: diffusion-weighting factor; c_{glc}: blood glucose concentration; c_{lac}: blood lactate concentration; CSI: chemical shift imaging; CT: computed tomography; DCE: dynamic contrast enhancement; DNP: dissolution dynamic polarization; DWI: diffusion-weighted imaging; $d_{t\text{-}v}$: distance between the vena cava and the center of mass of the tumors; EDTA: sodium ethylenediaminetetraacetic acid, EPI: "echo planar imaging; [^{18}F]FDG: 2-deoxy-2-[^{18}F]fluoro-D-glucose; FLASH: fast low-angle shot; FLAIR: fluid-attenuated inversion recovery; fMRI: functional magnetic resonance imaging; FOV: field of view; HASTE: half Fourier acquisition single shot turbo spin echo; H.E.: Hematoxylin-Eosin; HP: hyperpolarized; HyperPET: simultaneous ^{13}C-hyperpolarized magnetic resonance spectroscopic imaging and position emission tomography; IDIF: image derived input function; $I(lactate)_{tumor}$: summed mean lactate integrals in tumor ROIs; $I_{norm.}$: hyperpolarized pyruvate and lactate signals normalized by the maximum observed pyruvate signal; $I(pyruvate)_{tumor}$: summed mean pyruvate integrals in tumor ROIs; k_1: primary tracer uptake rate from blood to free tracer in tissue; k_2: tissue clearance rate; k_3: rates of exchange between free and trapped tracers in tissue; K_i: composite rate constant; k_{lp}: rate constant for lactate-pyruvate-exchange; k_{pl}: rate constant for pyruvate-lactate-exchange; $k_{pl,slice}$: rate constant for pyruvate-lactate-exchange measured in the whole CSI slice; kVp: peak kilovoltage; *LC*: lumped constant; LDH: lactate dehydrogenase; LDH-A: lactate dehydrogenase A; MAT-B-III: mammary breast cancer cells derived from adenocarcinoma; M_{lac}: observable magnetization of hyperpolarized lactate; MPRAGE: magnetization prepared rapid acquisition gradient echo; *MRGLU*: metabolic rate of glucose; MR: magnetic resonance; MRAC: magnetic resonance-based attenuation correction; MRI: magnetic resonance imaging; MRSI: magnetic resonance spectroscopic imaging; M_{pyr}: observable magnetization of hyperpolarized pyruvate; *n*: number or data points; NaOH: sodium hydroxide; NMR: nuclear magnetic resonance; OSEM: ordered subset expectation maximization; OX063: (tris(8-carboxy-2,2,6,6-tetra-(hydroxyethyl)-benzo-[1,2-4,5]-bis-(1,3)-dithiole-4-yl)-methyl sodium salt); *p*: significance level; PBS: phosphate buffered saline; PET: positron emission tomography; *R*: Pearson correlation coefficient; RF: radiofrequency; r_{inj}: injection rate; ROI: region-of-interest; RPMI-1640: Roswell Park Memorial Institute 1640 cell culture medium; *S*: signal intensity for a defined *b*-value; S_0: signal without diffusion-weighting; *std*: standard deviation *SUV*: standard uptake value; SUV_{max}: maximum standard uptake value; SUV_{mean}: mean of *SUV*s that are greater than SUV_{max} multiplied by a defined threshold (0.5 or 0.7) within a ROI; T_1: spin-lattice relaxation time; $T_{1lac,eff.}$: effective relaxation rate of hyperpolarized lactate; $T_{1pyr,eff.}$: effective relaxation rate of hyperpolarized pyruvate; T_2: spin-spin relaxation time; $t_{arr.}$: time of substrate arrival; *TE*: echo time; *TR*: repetition time; *TLG*: total lesion glycolysis; $t_{max,pyr}$: time of observed maximum of hyperpolarized pyruvate; *TMV*: tumor metabolic volume; UTE: ultra-short echo time; ρ_{lac}: effective decay rate of hyperpolarized lactate; ρ_{pyr}: effective decay rate of hyperpolarized pyruvate.

Supplementary Material

Supplementary information, figures and tables.
http://www.thno.org/v08p4765s1.pdf

Acknowledgments

We acknowledge Birgit Blechert and Michael Michalik for culturing cells, Sylvia Schachoff for her help with the PET/MR and Sybille Reder and Markus Mittelhäuser for performing the PET/CT measurements.

Author contributions

C.H. planned experiments, designed the PET/MR workflow, operated the polarizer, wrote and revised the manuscript. M.B. handled animals and B.F. helped with the tumor model. C.M. operated the PET/MR scanner, A. E. H. provided the ^{13}C-CSI sequence and reconstruction scripts. M. S. analyzed DWI data. S.D., F.S. helped with ^{13}C-analysis and J.C. wrote PET analysis software in Matlab. W.W. and K.S. performed histological analysis. S. J. G., A. H., J. B. H, A. K., S.G.N. and M.S. designed the research and revised the manuscript.

Grant Support

We thank Cambridge Isotope Laboratories Inc. for providing [1-^{13}C]pyruvate and appreciate support from EU (Grant No. 642773 and 294582) and from the Deutsche Forschungsgemeinschaft (DFG, German Research Foundation): 391523415, 68647618, HO-4604/2-1, SFB 824 and Excellence Cluster No. 306. We further thank the DFG Major Instrumentation Initiative PET/MR. JBH acknowledges support by Kiel University and the Medical Faculty for supporting the Molecular Imaging North Competence Center (MOIN CC) as core facility for imaging *in vivo*. MOIN CC was founded by a grant of the European Regional Development Fund (ERDF) and the Zukunftsprogramm Wirtschaft of Schleswig-Holstein (Project no. 122-09-053).

Competing Interests

The authors have declared that no competing interest exists.

References

1. Rosenkrantz AB, Friedman K, Chandarana H, Melsaether A, Moy L, Ding YS, et al. Current status of hybrid PET/MRI in oncologic imaging. AJR Am J Roentgenol. 2016; 206: 162-72.
2. Sauter AW, Wehrl HF, Kolb A, Judenhofer MS, Pichler BJ. Combined PET/MRI: one step further in multimodality imaging. Trends Mol Med. 2010; 16: 508-15.
3. Gaertner FC, Furst S, Schwaiger M. PET/MR: a paradigm shift. Cancer Imaging. 2013; 13: 36-52.
4. Kjaer A, Torigian DA. Clinical PET/MR imaging in oncology: future perspectives. PET Clin. 2016; 11: 489-93.
5. Cabello J, Ziegler SI. Advances in PET/MR instrumentation and image reconstruction. Br J Radiol. 2018; 91: 20160363.
6. Warburg O. On the origin of cancer cells. Science. 1956; 123: 309-14.
7. Cairns RA, Harris IS, Mak TW. Regulation of cancer cell metabolism. Nat Rev Cancer. 2011; 11: 85-95.
8. Gatenby RA, Gillies RJ. Why do cancers have high aerobic glycolysis? Nat Rev Cancer. 2004; 4: 891-9.
9. Golman K, Zandt RI, Lerche M, Pehrson R, Ardenkjaer-Larsen JH. Metabolic imaging by hyperpolarized ^{13}C-magnetic resonance imaging for in vivo tumor diagnosis. Cancer Res. 2006; 66: 10855-60.
10. Day SE, Kettunen MI, Gallagher FA, Hu DE, Lerche M, Wolber J, et al. Detecting tumor response to treatment using hyperpolarized ^{13}C-magnetic resonance imaging and spectroscopy. Nat Med. 2007; 13: 1382-7.
11. Vander Heiden MG, Cantley LC, Thompson CB. Understanding the Warburg effect: the metabolic requirements of cell proliferation. Science. 2009; 324: 1029-33.
12. Kurhanewicz J, Vigneron DB, Brindle K, Chekmenev EY, Comment A, Cunningham CH, et al. Analysis of cancer metabolism by imaging hyperpolarized nuclei: prospects for translation to clinical research. Neoplasia. 2011; 13: 81-97.
13. Serrao EM, Brindle KM. Potential clinical roles for metabolic imaging with hyperpolarized [1-^{13}C]pyruvate. Front Oncol. 2016; 6: 59.
14. Jensen MM, Erichsen KD, Johnbeck CB, Bjorkling F, Madsen J, Jensen PB, et al. [^{18}F]FDG and [^{18}F]FLT positron emission tomography imaging following treatment with belinostat in human ovary cancer xenografts in mice. BMC Cancer. 2013; 13: 168.
15. Johnbeck CB, Munk Jensen M, Haagen Nielsen C, Fisker Hag AM, Knigge U, Kjaer A. ^{18}F-FDG and ^{18}F-FLT-PET imaging for monitoring everolimus effect on tumor-growth in neuroendocrine tumors: studies in human tumor xenografts in mice. PLOS One. 2014; 9: e91387.
16. Phelps ME, Huang SC, Hoffman EJ, Selin C, Sokoloff L, Kuhl DE. Tomographic measurement of local cerebral glucose metabolic rate in humans with (^{18}F)-2-fluoro-2-deoxy-D-glucose: validation of method. Ann Neurol. 1979; 6: 371-88.
17. Blodgett TM, Meltzer CC, Townsend DW. PET/CT: form and function. Radiology. 2007; 242: 360-85.
18. Haberkorn U, Markert A, Mier W, Askoxylakis V, Altmann A. molecular imaging of tumor metabolism and apoptosis. Oncogene. 2011; 30: 4141.
19. Glunde K, Bhujwalla ZM, Ronen SM. Choline metabolism in malignant transformation. Nat Rev Cancer. 2011; 11: 835-48.
20. Ardenkjaer-Larsen JH, Fridlund B, Gram A, Hansson G, Hansson L, Lerche MH, et al. Increase in signal-to-noise ratio of > 10,000 times in liquid-state NMR. Proc Natl Acad Sci USA. 2003; 100: 10158-63.
21. Nelson SJ, Kurhanewicz J, Vigneron DB, Larson PEZ, Harzstark AL, Ferrone M, et al. Metabolic imaging of patients with prostate cancer using hyperpolarized [1-^{13}C]pyruvate. Sci Transl Med. 2013; 5: 198ra08-ra08.
22. Serrao EM, Kettunen MI, Rodrigues TB, Lewis DY, Gallagher FA, Hu DE, et al. Analysis of ^{13}C and ^{14}C labeling in pyruvate and lactate in tumor and blood of lymphoma-bearing mice injected with ^{13}C- and ^{14}C-labeled pyruvate. NMR Biomed. 2018; 31: 5: e3901.
23. Doherty JR, Cleveland JL. Targeting lactate metabolism for cancer therapeutics. J Clin Invest. 2013; 123: 3685-92.
24. Kettunen MI, Hu DE, Witney TH, McLaughlin R, Gallagher FA, Bohndiek SE, et al. Magnetization transfer measurements of exchange between hyperpolarized [1-^{13}C]pyruvate and [1-^{13}C]lactate in a murine lymphoma. Magn Reson Med. 2010; 63: 872-80.
25. Gutte H, Hansen AE, Larsen MM, Rahbek S, Henriksen ST, Johannesen HH, et al. Simultaneous hyperpolarized ^{13}C-pyruvate MRI and ^{18}F-FDG PET (HyperPET) in 10 dogs with cancer. J Nucl Med. 2015; 56: 1786-92.
26. Gutte H, Hansen AE, Henriksen ST, Johannesen HH, Ardenkjaer-Larsen J, Vignaud A, et al. Simultaneous hyperpolarized ^{13}C-pyruvate MRI and ^{18}F-FDG-PET in cancer (hyperPET): feasibility of a new imaging concept using a clinical PET/MRI scanner. Am J Nucl Med Mol Imaging. 2015; 5: 38-45.
27. Hansen AE, Andersen FL, Henriksen ST, Vignaud A, Ardenkjaer-Larsen JH, Højgaard L, et al. Simultaneous PET/MRI with ^{13}C-magnetic resonance spectroscopic imaging (hyperPET): phantom-based evaluation of PET quantification. EJNMMI Phys. 2016; 3: 7.
28. Hansen AE, Gutte H, Holst P, Johannesen HH, Rahbek S, Clemmensen AE, et al. Combined hyperpolarized ^{13}C-pyruvate MRS and ^{18}F-FDG PET (hyperPET) estimates of glycolysis in canine cancer patients. Eur J Radiol. 2018; 103: 6-12.
29. Witney TH, Kettunen MI, Day SE, Hu DE, Neves AA, Gallagher FA, et al. A comparison between radiolabeled fluorodeoxyglucose uptake and hyperpolarized ^{13}C-labeled pyruvate utilization as methods for detecting tumor response to treatment. Neoplasia. 2009; 11: 574-82.
30. Menzel MI, Farrell EV, Janich MA, Khegai O, Wiesinger F, Nekolla S, et al. Multimodal assessment of in vivo metabolism with hyperpolarized [1-^{13}C]MR spectroscopy and ^{18}F-FDG PET imaging in hepatocellular carcinoma tumor-bearing rats. J Nucl Med. 2013; 54: 1113-9.
31. Ravoori MK, Singh SP, Lee J, Bankson JA, Kundra V. In vivo assessment of ovarian tumor response to tyrosine kinase inhibitor pazopanib by using hyperpolarized ^{13}C-pyruvate MR spectroscopy and ^{18}F-FDG PET/CT imaging in a mouse model. Radiology. 2017; 285: 830-8.
32. Greve DN, Salat DH, Bowen SL, Izquierdo-Garcia D, Schultz AP, Catana C, et al. Different partial volume correction methods lead to different conclusions: an ^{18}F-FDG PET study of aging. Neuroimage. 2016; 132: 334-43.
33. Herneth AM, Guccione S, Bednarski M. Apparent diffusion coefficient: a quantitative parameter for in vivo tumor characterization. Eur J Radiol. 2003; 45: 208-13.
34. Hamacher K, Coenen HH, Stocklin G. Efficient stereospecific synthesis of no-carrier-added 2-[^{18}F]-fluoro-2-deoxy-D-glucose using aminopolyether supported nucleophilic substitution. J Nucl Med. 1986; 27: 235-8.
35. Chen HH, Chiu NT, Su WC, Guo HR, Lee BF. Prognostic value of whole-body total lesion glycolysis at pretreatment FDG PET/CT in non-small cell lung cancer. Radiology. 2012; 264: 559-66.
36. Kim TM, Paeng JC, Chun IK, Keam B, Jeon YK, Lee SH, et al. Total lesion glycolysis in positron emission tomography is a better predictor of outcome than the international prognostic index for patients with diffuse large B cell lymphoma. Cancer. 2013; 119: 1195-202.
37. Patlak CS, Blasberg RG, Fenstermacher JD. Graphical evaluation of blood-to-brain transfer constants from multiple-time uptake data. J Cereb Blood Flow Metab. 1983; 3: 1-7.
38. Hundshammer C, Düwel S, Ruseckas D, Topping G, Dzien P, Müller C, et al. Hyperpolarized amino acid derivatives as multivalent magnetic resonance pH sensor molecules. Sensors. 2018; 18: 2.
39. Durst M, Koellisch U, Frank A, Rancan G, Gringeri CV, Karas V, et al. Comparison of acquisition schemes for hyperpolarised ^{13}C-imaging. NMR Biomed. 2015; 28: 715-25.
40. Hill DK, Orton MR, Mariotti E, Boult JKR, Panek R, Jafar M, et al. Model free approach to kinetic analysis of real-time hyperpolarized ^{13}C-magnetic resonance spectroscopy data. PLOS ONE. 2013; 8: e71996.
41. Doblas S, Almeida GS, Ble FX, Garteiser P, Hoff BA, McIntyre DJ, et al. Apparent diffusion coefficient is highly reproducible on preclinical imaging systems: evidence from a seven-center multivendor study. J Magn Reson Imaging. 2015; 42: 1759-64.
42. Westin CF, Maier SE, Mamata H, Nabavi A, Jolesz FA, Kikinis R. Processing and visualization for diffusion tensor MRI. Med Image Anal. 2002; 6: 93-108.
43. Koh DM, Collins DJ. Diffusion-weighted MRI in the body: applications and challenges in oncology. AJR Am J Roentgenol. 2007; 188: 1622-35.
44. Padhani AR, Liu G, Mu-Koh D, Chenevert TL, Thoeny HC, Takahara T, et al. Diffusion-weighted magnetic resonance imaging as a cancer biomarker: consensus and recommendations. Neoplasia. 2009; 11: 102-25.
45. Cohen J. Statistical power analysis for the behavioral sciences. New York, USA: Academic Press; 1977.

46. Longo DL, Bartoli A, Consolino L, Bardini P, Arena F, Schwaiger M, et al. In vivo imaging of tumor metabolism and acidosis by combining PET and MRI-CEST pH imaging. Cancer Res. 2016; 76: 6463-70.
47. Thackeray JT, Bankstahl JP, Bengel FM. Impact of image-derived input function and fit time intervals on Patlak quantification of myocardial glucose uptake in mice. J Nucl Med. 2015; 56: 1615-21.
48. Lanz B, Poitry-Yamate C, Gruetter R. Image-derived input function from the vena cava for ^{18}F-FDG PET studies in rats and mice. J Nucl Med. 2014; 55: 1380-8.
49. Skoch A, Jiru F, Bunke J. Spectroscopic imaging: basic principles. Eur J Radiol. 2008; 67: 230-9.
50. Delso G, Furst S, Jakoby B, Ladebeck R, Ganter C, Nekolla SG, et al. Performance measurements of the Siemens mMR integrated whole-body PET/MR scanner. J Nucl Med. 2011; 52: 1914-22.
51. Wu C, Li F, Niu G, Chen X. PET imaging of inflammation biomarkers. Theranostics. 2013; 3: 448-66.
52. Seitz BM, Krieger-Burke T, Fink GD, Watts SW. Serial measurements of splanchnic vein diameters in rats using high-frequency ultrasound. Front Pharmacol. 2016; 7: 116.
53. Constantinescu CC, Mukherjee J. Performance evaluation of an Inveon PET preclinical scanner. Phys Med Biol. 2009; 54: 2885-99.
54. Wang H, Cao Y. Correction of arterial input function in dynamic contrast-enhanced MRI of the liver. J Magn Reson Imaging. 2012; 36: 411-21.
55. Shimoji K, Ravasi L, Schmidt K, Soto-Montenegro ML, Esaki T, Seidel J, et al. Measurement of cerebral glucose metabolic rates in the anesthetized rat by dynamic scanning with ^{18}F-FDG, the ATLAS small animal PET scanner, and arterial blood sampling. J Nucl Med. 2004; 45: 665-72.
56. Kazan SM, Reynolds S, Kennerley A, Wholey E, Bluff JE, Berwick J, et al. Kinetic modeling of hyperpolarized ^{13}C pyruvate metabolism in tumors using a measured arterial input function. Magn Reson Med. 2013; 70: 943-53.
57. Wiesinger F, Weidl E, Menzel MI, Janich MA, Khegai O, Glaser SJ, et al. IDEAL spiral CSI for dynamic metabolic MR imaging of hyperpolarized [1-^{13}C]pyruvate. Magn Reson Med. 2012; 68: 8-16.
58. Reed GD, Larson PEZ, von Morze C, Bok R, Lustig M, Kerr AB, et al. A method for simultaneous echo planar imaging of hyperpolarized ^{13}C pyruvate and ^{13}C lactate. J Magn Reson. 2012; 217: 41-7.
59. Hay N. Reprogramming glucose metabolism in cancer: can it be exploited for cancer therapy? Nat Rev Cancer. 2016; 16: 635-49.
60. Gu J, Khong P-L, Wang S, Chan Q, Law W, Zhang J. Quantitative assessment of diffusion-weighted MR imaging in patients with primary rectal cancer: correlation with FDG-PET/CT. Mol Imaging Biol. 2011; 13: 1020-8.
61. Schmidt H, Brendle C, Schraml C, Martirosian P, Bezrukov I, Hetzel J, et al. Correlation of simultaneously acquired diffusion-weighted imaging and 2-deoxy-[^{18}F] fluoro-2-D-glucose positron emission tomography of pulmonary lesions in a dedicated whole-body magnetic resonance/positron emission tomography system. Invest Radiol. 2013; 48: 247-55.
62. Brandmaier P, Purz S, Bremicker K, Höckel M, Barthel H, Kluge R, et al. Simultaneous [^{18}F]FDG-PET/MRI: correlation of apparent diffusion coefficient (ADC) and standardized uptake value (SUV) in primary and recurrent cervical cancer. PLOS ONE. 2015; 10: e0141684.
63. Andersen LW, Mackenhauer J, Roberts JC, Berg KM, Cocchi MN, Donnino MW. Etiology and therapeutic approach to elevated lactate. Mayo Clin Proc. 2013; 88: 1127-40.